Quantitative Analysis of Spectral Interference of Spontaneous Raman Scattering in High-Pressure Fuel-Rich H₂–Air Combustion

JUN KOJIMA[*] AND QUANG-VIET NGUYEN

NASA GLENN RESEARCH CENTER, CLEVELAND OH 44135

[*] Corresponding author: National Research Council resident research associate. Current address: OAI, 22800 Cedar Point Rd, Cleveland, OH 44142. Phone: (440) 962-3095, Fax: (440) 962-3120, Jun.Kojima@grc.nasa.gov.

Key Words: Combustion diagnostics; High-pressure flame; Raman scattering; Spectral interference; Raman spectral simulation

Abstract

We present a theoretical study of the spectral interferences in the spontaneous Raman scattering spectra of major combustion products in 30-atm fuel-rich hydrogen–air flames. An effective methodology is introduced to choose an appropriate line-shape model for simulating Raman spectra in high-pressure combustion environments. The Voigt profile with the additive approximation assumption was found to provide a reasonable model of the spectral line shape for the present analysis. The rotational/vibrational Raman spectra of H_2, N_2, and H_2O were calculated using an anharmonic-oscillator model using the latest collisional broadening coefficients. The calculated spectra were validated with data obtained in a 10-atm fuel-rich H_2– air flame and showed excellent agreement. Our quantitative spectral analysis for equivalence ratios ranging from 1.5 to 5.0 revealed substantial amounts of spectral cross-talk between the rotational H_2 lines and the N_2 O-/Q-branch; and between the vibrational H_2 $O(0,3)$ line and the vibrational H_2O spectrum. We also address the temperature dependence of the spectral cross-talk and extend our analysis to include a cross-talk compensation technique that removes the interference arising from the H_2 Raman spectra onto the N_2, or H_2O spectra.

1. Introduction

Quantitative measurements of species concentration and temperature in elevated pressure combustion environments are critical to the validation of computer models used in the development of gas turbine and internal combustion engines. Laser-excited Spontaneous Raman scattering (SRS) spectroscopy is perhaps the only practical technique that provides spatially and temporally resolved multi-species information in a simultaneous or single-shot fashion with a high level of accuracy [1-3]. For high pressure combustion studies, SRS has the added benefit of providing stronger signal levels than those performed at atmospheric pressure, because the signal scales linearly with the number density, and hence pressure of the molecules being probed. Furthermore, SRS measurements are relatively simple, less expensive, and more versatile when compared to coherent anti-Stokes Raman spectroscopy (CARS), or stimulated Raman spectroscopy. These facts have motivated a recent renewed interest in fundamental studies that apply SRS diagnostics in high-pressure combustion [4-5].

Although the use of SRS diagnostics for quantitative studies in flame studies is well known, special attention to spectral interferences between Raman scattering from different molecules will still require further study. This requirement is substantiated by the fact that several earlier studies have indicated that spectral interferences can be a significant problem for Raman diagnostics in flames [2-3,6-8]. In fact, the use of a detailed spectral analysis that includes the spectral interferences or 'cross-talk' between different vibrational/rotational Raman bands of different molecular species, is the basis for several common SRS techniques including thermometry via Stokes/anti-Stokes ratio [9], and integrated area measurements of vibrational Raman bands for species concentrations [10]. Without considering the spectral interferences among the different Raman bands for multiple species, the accuracy of temperature/species measurements is insufficient for combustion model validation.

The effect of spectral interferences on the SRS signals has been effectively implemented using the well-known cross-talk matrix calibration procedure [2-3,6-8]. The off-diagonal terms of the calibration matrix generally represent the Raman scattering crosstalk of one species onto another. The acquisition and development of an accurate cross-talk calibration matrix is the key factor in obtaining quantitative species

concentration and temperature measurements in flames. Unfortunately, the Raman cross-talk calibration data obtained from these one-of-a-kind setups to date is not easily convertible into a transferable standard that is suitable for use by other researchers, particularly those who deal with high-pressure flames. In order to create a standardized cross-talk calibration matrix with absolute numbers, a comprehensive and accurate study of the spectral interference among Raman scattering in flames of various conditions (fuel-air composition, equivalence ratio, and temperature) over a range of *pressure* is still required.

The quantitative treatment of the spectral interference in flames is not an easy task since the interference is a molecule-dependent function of temperature, species concentration, and chemical composition. For instance, rotational H_2 Raman lines at rotational quantum number, $J = 9$ to $J = 11$ around the 2300 cm^{-1} Raman shift in fuel-rich hydrogen flames may become strong enough to interfere with the N_2 Q-branch spectrum (near 2330 cm^{-1}). In particular, the rotational $J = 10$ Stokes line of H_2 is completely overwhelmed by the N_2 Q-branch. In order to facilitate the quantitative analysis of these interferences, a theoretical means of predicting the SRS spectra is essential. The quantitative analysis of the interferences are even further complicated in high-pressure flames due to possible pressure broadening or collisional line-narrowing effects [11].

In this paper, we investigate the spectral interferences between combustion molecules in high-pressure, fuel-rich, hydrogen–air flames using a spectral simulation of the SRS process. We focus our attention in this paper to hydrogen-air flames for the following reasons: chemically, a H_2–air flame provides the simplest combination of combustion products in order to facilitate the spectral analysis, yet retains spectral features that are important to more complicated fuel-oxidizer systems that will be studied at a later time; research data on a H_2–air flames are important in high-speed propulsion systems such as rocket combustors and pulse detonation engines. Fuel-rich hydrogen flames are studied here because they are typically used in rocket engines for reasons of flame stability and maximum heat-release. Furthermore, the interference between H_2 and other molecules becomes important in fuel-rich flames where H_2 concentration is high.

We first introduce an analytical methodology to validate an appropriate line-shape model for simulating Raman spectra in high-pressure flames and compare it with experimental data to verify our theoretical model for simulating Raman spectra. We then model the rotational/vibrational Raman spectra of H_2, N_2, and H_2O using an anharmonic-oscillator model with a line-shape model that incorporates the latest collisional broadening coefficient data. Finally, we theoretically investigate the spectral behavior of Raman O-, S-, and Q-branches of the species in hypothetical high-pressure hydrogen flames over a range of equivalence ratios.

2. Modeling of Raman Spectra

2-1. Raman Cross-Section

The theory of Raman scattering in diatomic and polyatomic molecules is well established [12]. According to Placzek's polarization theory of the Raman effect, the corresponding differential Raman scattering cross-section per molecule at thermal equilibrium is given by [12]

$$\left(\frac{\partial\sigma}{\partial\Omega}\right)^{\theta}_{i\rightarrow f} = \left(\frac{\pi}{\varepsilon_0}\right)^2 (v_0 \pm v_k)^4 g\frac{\exp(-E_i/kT)}{Q(T)}\Phi(\alpha^2,\beta^2,\theta)f(J). \tag{1}$$

Here, the superscript θ indicates the relative angle of the planes of polarization between scattered and incident light; the subscripts of i and f represent the initial and final states respectively; ε_0 is the vacuum permittivity; v_0 is the incident light (laser) frequency; $+$ and $-$ signs refer to the anti-Stokes and Stokes Raman scattering respectively; v_k is the molecular frequency associated with the rotation-vibration, or the pure rotational transition from i to f; g is the total degeneracy; E_i is the energy of the initial state; k is the Boltzmann constant; T is the gas temperature; $Q(T)$ is the total partition function of the molecule at temperature T; $\Phi(\alpha^2, \beta^2,\theta)$ is the molecule-dependent temperature-independent invariant that is a function of the mean value of the derived polarizability

tensor α^2 and the anisotropy tensor β^2. The values for $\Phi(\alpha^2, \beta^2, \theta)$ are tabulated by Long [12] for every branch of vibrational and pure rotational scattering for the molecules of interest; and $f(J)$ is the correction factor arising from the rotation-vibration coupling [13]. Note that Eq. (1) should be multiplied by the factors $(v + 1)b_v^2$ and vb_v^2 for vibrational Stokes and anti-Stokes scattering of a diatomic molecule, respectively. Here, v is the vibrational quantum number and b_v^2 is defined as $h/8\pi^2 c v_k$ where h is the Plank constant, and c is the speed of light.

The Raman line frequency is given by $v_k = (E_f - E_i)/hc$ where E_f is the energy of the final state. The energy in a rovibrational state (v, J) is expressed as the sum of the vibrational energy term, $G(v)$ and the rotational energy term, $F(v, J)$

$$E(v,J) = hc[G(v) + F(v,J)]. \tag{2}$$

According to the anharmonic oscillator model, the vibrational energy term $G(v)$ of a diatomic molecule is given by [14]

$$G(v) = \omega_e\left(v + \frac{1}{2}\right) - \omega_e x_e\left(v + \frac{1}{2}\right)^2 + \omega_e y_e\left(v + \frac{1}{2}\right)^3 \tag{3}$$

where ω_e, $\omega_e x_e$, and $\omega_e y_e$ are the molecular constants and are tabulated by Huber and Hertzberg [15]. According to the non-rigid rotator model that accounts for the influence of the centrifugal distortion, the rotational term for the $^1\Sigma$ (singlet) state of diatomic molecules such as N_2 or H_2 is given by

$$F(v,J) = B_v J(J+1) - D_v J^2(J+1)^2 + H_v J^3(J+1)^3 \tag{4}$$

where $B_v = B_e - \alpha_e(v + \frac{1}{2}) + \gamma_e(v + \frac{1}{2})^2 - \eta_e(v + \frac{1}{2})^3$, $D_v = D_e + \beta_e(v + \frac{1}{2}) + \xi_e(v + \frac{1}{2})^2$, and $H_v = H_e - \zeta_e(v + \frac{1}{2})$. The terms B_e, D_e, H_e, α_e, β_e, γ_e, η_e, ξ_e, and ζ_e are the molecular-

dependent spectroscopic constants, which are tabulated for each molecule of interest by Huber and Hertzberg [15]. Thus for a Stokes branch ($\Delta v = v_f - v_i = +1$), the Raman line frequency is given by

$$v_k(v_i, J_i) = \frac{E(v_i + 1, J_f) - E(v_i, J_i)}{hc} .$$

(5)

The partition function $Q(T)$ for a rovibronic state may be written as the sum of the rotational and the vibrational partition functions

$$Q(T) = Q_{vib}(T) + Q_{rot}(T)$$

(6)

where

$$Q_{vib}(T) = \sum_{v=0}^{\infty} \exp\left(\frac{-hcG(v)}{kT}\right),$$

(7)

$$Q_{rot}(T) = \sum_{v=0}^{\infty} \sum_{J=0}^{\infty} g_s (2J+1) \exp\left(\frac{-hcF(v,J)}{kT}\right).$$

(8)

Here g_s is the nuclear spin statistical weight and the term $(2J + 1)$ is the rotational degeneracy.

For calculating a pure rotational Raman spectrum (e.g. rotational H_2 *S*-branch), Eqs. (2), (5), and (6) are replaced by $E(J) = hcF(J)$ where $F(J) = F(0, J)$, $v_k(J_i) = [E(J_f) - E(J_i)]/hc$, and $Q(T) = Q_{rot}(T)$, respectively.

The correction factor $f(J)$ is given by

$$f(J_i) = 1 + 4\chi^{-1}(B_e/\omega_e)^2 \left[J_i(J_i + 1) + J_f(J_f + 1)\right] ,$$

(9)

where χ^{-1} is the polarizability-related spectroscopic term. The values of χ^{-1} for N_2, and H_2 have been found to be 2.5 [13]. The factor $f(J)$ is substantial for N_2 at temperature above 1000 K and is significant for H_2 because of its large rotational constant [13].

Polarizability Tensor Components

According to Placzek-Teller theory, the space-averaged $\Phi(\alpha^2, \beta^2, \theta)$ terms for the Raman Q-, O-, and S-branches for scattered light that is polarized along the direction of the incident light polarization are given by the following equations, respectively [12,16-17]:

$$\Phi(\alpha,\beta)_Q = \left|\langle \psi_{v,J} \mid \alpha \mid \psi_{v+1,J}\rangle\right|^2 + \frac{4}{45} S_{J,J}\left|\langle \psi_{v,J} \mid \beta \mid \psi_{v+1,J}\rangle\right|^2, \tag{10}$$

$$\Phi(\alpha,\beta)_O = \frac{4}{45} S_{J-2,J}\langle \psi_{v,J} \mid \beta \mid \psi_{v+1,J-2}\rangle, \tag{11}$$

$$\Phi(\alpha,\beta)_S = \frac{4}{45} S_{J+2,J}\langle \psi_{v,J} \mid \beta \mid \psi_{v+1,J+2}\rangle, \tag{12}$$

where $\psi_{v,J}$ is the vibrational wavefunction for a particular v-J state; α is the isotropic part of the polarizability, and β is the anisotropic part of the polarizability. $S_{J',J''}$ are the Placzek-Teller coefficients for diatomic molecules given by [1,12]

$$S_{J,J} = \frac{J(J+1)}{(2J-1)(2J+3)} \quad (Q\text{-branch}), \tag{13}$$

$$S_{J,J-2} = \frac{3J(J-1)}{2(2J+1)(2J-1)} \quad (O\text{-branch}), \tag{14}$$

$$S_{J+2,J} = \frac{3(J+1)(J+2)}{2(2J+1)(2J+3)} \quad (S\text{-branch}). \tag{15}$$

Evaluation of Eqs. (10-12) based on the reasonable approximation for vibrational transitions with $\Delta v = 1$ yields [16]

$$\Phi(\alpha,\beta)_Q = (B_e/\omega_e)\left(\alpha'^2 + \frac{4}{45}S_{J,J}\beta'^2 \right), \tag{16}$$

$$\Phi(\alpha,\beta)_O = (B_e/\omega_e)\frac{4}{45}S_{J,J-2}\beta'^2, \tag{17}$$

$$\Phi(\alpha,\beta)_S = (B_e/\omega_e)\frac{4}{45}S_{J+2,J}\beta'^2. \tag{18}$$

Substituting Eqs. (16-18) into Eq. (1) and evaluating the degeneracy terms we obtain the following relations:

$$\left(\frac{\partial\sigma}{\partial\Omega}\right)_Q^{ZZ} = q(\nu_0 \pm \nu_k)^4(2J+1)g_s\,\frac{\exp(-E_{is}/kT)}{Q(T)}\left[\frac{45}{4}\left(\frac{\alpha'}{\beta'}\right)^2 + S_{J,J}\right]f(J), \tag{19}$$

$$\left(\frac{\partial\sigma}{\partial\Omega}\right)_O^{ZZ} = q(\nu_0 \pm \nu_k)^4(2J+1)g_s\,\frac{\exp(-E_{is}/kT)}{Q(T)}S_{J,J-2}f(J), \tag{20}$$

$$\left(\frac{\partial\sigma}{\partial\Omega}\right)_S^{ZZ} = q(\nu_0 \pm \nu_k)^4(2J+1)g_s\,\frac{\exp(-E_{is}/kT)}{Q(T)}S_{J+2,J}f(J), \tag{21}$$

where the superscript ZZ indicates the scattered light polarized along the direction of the incident light polarization; q is a molecule-independent physical constant; g_s is the nuclear spin statistical weight ($g_s = 1$ for even J; $g_s = 3$ for odd J); ($2J+1$) is the rotational degeneracy. The terms α' and β' are the isotropic (mean) and anisotropic invariants of the static dipole polarizability derivatives, which are derived from the expansion in the

dimensionless vibrational coordinate $\xi \equiv (r-r_e)/r_e$ (where r is the internuclear distance and r_e is the equilibrium internuclear distance) [16-17],

$$\alpha = \alpha_0 + \alpha'\xi + \frac{1}{2}\alpha''\xi^2 + \ldots, \tag{22}$$

$$\beta' = \beta_0 + \beta'\xi + \frac{1}{2}\beta''\xi^2 + \ldots, \tag{23}$$

with

$$\alpha' = \partial\alpha / \partial\xi \mid_{\xi=0}, \tag{24}$$

$$\beta' = \partial\beta / \partial\xi \mid_{\xi=0}. \tag{25}$$

H₂O Raman Model

The Raman scattering spectrum of water vapor appears over the range of frequency from 3400 to 4130 cm^{-1}, and results mainly from the OH-stretch vibrational mode. Generally, the temperatures encountered in combustion environments makes the ν_1 band (100)-(000) transition dominant. For the H_2O Raman spectrum, the classical anharmonic-oscillator model is not suitable for calculating the vibrational energy because of the asymmetric top nature of the water molecule that shows a relatively complicated structure. Fortunately, the vibrational energies in the vibrational ground state (000), and in the various excited states such as the (100), and (001) are known from the analysis of a high-resolution infrared spectrum and such database is tabulated in HITRAN [18]. The wavefunctions for those states were also calculated based on the rotational Hamiltonian by Flaud *et al* [19] that includes the Fermi resonance between the (100) and (020) states, and the Coriolis-like anharmonic coupling between these two states and the (001) state. Based on the wavefunctions and the polarizability derivatives, Avila *et al* [20] calculated the vibrational Raman cross-sections of H_2O in the OH-stretching region with great accuracy

up to about 1000 K. In the current report, we then used the results on the Raman line frequency and cross-sections which are tabulated in Ref. 20 to simulate the H_2O Raman spectra in our high-pressure flames.

The partition function of H_2O was calculated using the well known polynomial expression [18,21]

$$Q(T) = a + bT + cT^2 + dT^3, \qquad (26)$$

where coefficients a, b, c, and d are tabulated over the range of temperature up to 3005 K by Gamache [21].

It should be noted that the resulting calculated H_2O Raman spectrum does not include the hot bands of the (110)-(010) and (011)-(010) transitions that become important over 1500 K as well as the additional hot bands from the (020)-(000), (100)-(000), and (001)-(000), which would appear at higher temperature as Avila *et al* [20] give caution. These hot bands generally "stretch" a H_2O spectrum out to the shorter wavelength, thus they form a longer blue-side tail. According to Avila *et al* [20], the intensities of these hot bands amount to over 10% of that of the main bands so that the present calculation for H_2O, likely, also has errors of this level at higher temperature conditions.

2-2. Line-Shape

Pressure-Broadening Coefficient

Collisional broadening coefficients of molecules are a dominant factor for the line-shape modeling. Recently collisional broadening coefficients for H_2 with perturber molecules have been proposed by advanced line-shape calculations and those numbers over a range of temperature and pressure have been successfully applied to CARS thermometry in high-pressure flames [22-24]. Bergmann *et al* [22] obtained J-dependent H_2 collisional broadening coefficients for higher temperature from 1800 to 2200 K for $J = 0$ to 7 in a fuel-rich CH_4–air flame up to 40 bar. Hussong *et al* [23] provided an effective, J-

dependent polynomial equation for the H_2 collisional broadening coefficient including the inhomogeneous contribution (nonlinear dependence on the perturber concentration) in the H_2–N_2 binary system:

$$\tilde{\gamma}_J^0(T,C) = (\gamma_0^{\text{self}})_J + (\tilde{\gamma}^{\text{self}})_J T + (a_1)_J C + (a_2)_J C^2 + (a_3)_J CT + (a_4)_J C^2 T, \qquad (27)$$

where $\tilde{\gamma}_J^0$ [cm^{-1}/atm] is the total broadening coefficient as a function of temperature, T and concentration of perturber N_2, C. Here C is defined by the N_2 fraction relative to H_2 concentration under the assumption of the H_2–N_2 binary system. All other parameters, $(\gamma_0^{\text{self}})_J$, $(\tilde{\gamma}^{\text{self}})_J$, $(a_i)_J$ (i = 1 to 4) are tabulated for J = 0 to 5 in Ref. 23.

Since the influence of H_2O as an additional collider plays an important role at higher temperature in terms of speed-inhomogeneous effects as Hussong *et al* [23-24] mentioned in their reports, a ternary system H_2-N_2-H_2O should be considered for better accuracy over the range of flame temperature. Unfortunately, the collisional broadening coefficients of ternary mixture including H_2O at high temperature have not yet been reported in the literature. We thus calculated the H_2 broadening coefficient for each flame condition using Eq. (27) in this study. Furthermore, in an effort to simplify the effects of temperature and J-number dependence on the collisional broadening for hydrogen, we use the broadening coefficient of J = 3 for all lines in the H_2 spectrum. Note that the above-mentioned assumption regarding the binary system and the single-value coefficient has been previously found to be both appropriate and practical from a diagnostics standpoint [25].

There is an alternative expression for the collisional broadening coefficient, which has been proposed in the HITRAN database [18]. Molecular spectroscopic information (including the collisional broadening coefficients) of major combustion-related species such as N_2 or H_2O are available in the database while there is no information regarding H_2, due to the fact that it is not an infrared active molecule. We then used HITRAN [18] to find spectroscopic information for the collisional broadening coefficients of N_2 and H_2O. In the database, the collisional broadened halfwidth is written as

$$\tilde{\gamma}_J^0(T,C)^{\text{HITRAN}} = \left(\frac{T_0}{T}\right)^n \left[\gamma^{\text{air}}(P_0,T_0)C + \gamma^{\text{self}}(P_0,T_0)(1-C)\right] \quad, \qquad (28)$$

where $\gamma^{\text{air}}(P_0,T_0)$, and $\gamma^{\text{self}}(P_0,T_0)$ are the air-broadened, and the self-broadened width at the reference temperature, $T_0 = 296$ K and the reference pressure, $P_0 = 1$ atm, and n is the coefficient of temperature dependence. As for N_2, only $\gamma^{\text{self}}(P_0,T_0)$ was considered and it was assumed to a single value of 0.048 cm^{-1}/atm. This value was derived from HITRAN by calculating an intensity-weighted, averaged halfwidth of all N_2 Q-branch lines from J = 1 to 40 in the vibrational 1-0 transition, which is the dominant transition at room temperature. For the H_2O lines, we used the widths given by $\gamma^{\text{air}}(P_0,T_0) = 0.0095$ and $\gamma^{\text{self}}(P_0,T_0) = 0.0923$, which were also derived from the HITRAN database by calculating an average halfwidth of all lines in the vibrational transition (000)-(100) between 3400 to 3710 cm^{-1} at room temperature. A value of $n = 0.5$ was used for N_2 according to Ref. 18 and $n = 0.67$ was found reasonable for H_2O after calculating an averaged n value for the (000)-(100) transition.

Process of Line-Shape Model Selection

Spectral line shapes of Raman scattering spectra at atmospheric pressure are typically modeled by a Gaussian profile, and those at higher pressures are usually modeled by a Voigt profile which is the convolution of Gaussian and Lorentzian collisional broadening distributions. However, the Voigt profile is based on the impact approximation, so it may not be valid for modeling spectral shapes at very high pressures due to the break down of the approximations in the far wings of spectral lines [27]. In some cases that require higher accuracy, such as in a laser absorption technique, motionally-narrowed Galatry profiles [26] could be also employed. These line-shape models were developed for a single isolated transition. In practice however, multiple overlapping transitions are common and the effect of their overlap may become important at high pressures. Thus, consideration of the line-narrowing due to the interaction between different transitions, the so-called line-mixing effect, may be required to properly model the Raman spectra for

quantitative measurements. The line-mixing effect in nonlinear Raman processes of pure gases at high pressure has been previously studied [11,28] but not in flames.

Based on the above points, we see the need to develop a methodology to choose an appropriate high-pressure line-shape model for a particular species, and to evaluate the limitations of these models. Nagali [29] discussed the applicability of the major line-shape models and introduced an effective approach for choosing an appropriate model for neutral species within the temperature and pressure range of interest. In this study, we follow the the approach described by Nagali [29] but include, for the first time, N_2 concentration-dependent collisional broadening coefficients to the analysis. This permits the determination of an appropriate collisional broadening model for simulating Raman spectra in high-pressure flames.

We consider three criteria for modeling the spectral lineshapes of Raman scattering spectra: 1) Motional narrowing (in which the Galatry profile is considered); 2) Impact approximation (in which the Voigt profile is valid); and 3) Line mixing (in which the additive approximation is not valid). To define the effectiveness and limitation of each criterion in terms of the range of temperature and pressure, we first define a collisional scale factor, i.e. the molecular collision duration, t_{coll} [s]. When the interaction length is set to the radius of the collision-broadening cross-section, t_{coll} can be expressed as

$$t_{coll}(T,C) = \frac{1}{v_{mol}} \sqrt{\frac{c \cdot \Delta v_c^0}{v_{mol} N_j}} \quad , \tag{29}$$

where Δv_c^0 [cm^{-1}] is the collisional broadening fullwidth which is twofold of the total broadening coefficient $\tilde{\gamma}_j^0$ at room temperature and atmospheric pressure, c [m/s] is the speed of light, N_j [cm^{-3}] is the number density of the molecule of species j; and v_{mol} [m/s] is the mean speed of the gas molecule which is approximately equal to another measure of the molecular speed, root-mean-square speed [30]

$$v_{\text{mol}}(T) = \sqrt{\frac{3RT}{M}} \quad , \tag{30}$$

where R [J K^{-1} mol^{-1}] is the gas constant, M [g mol^{-1}] is the molecular mass.

The wavelength region over which the impact approximation (collisional broadening due to intermolecular collisions which can be described by Lorentzian profile) is valid can be determined using the expression [31]

$$2\pi ct_{\text{coll}} \Delta v_{\text{imp}} \ll 1 \quad , \tag{31}$$

where Δv_{imp} is the spectral region in which the impact approximation is accurate. Thus, in the impact approximation region, Δv_{imp} can be written as

$$\Delta v_{\text{imp}}(T,C) = \frac{0.1}{2\pi ct_{\text{coll}}} . \tag{32}$$

Here we use a factor of 0.1, which is a smaller value than that suggested by Nagli (0.2) [29]. However, the exact value for this quantity is still open to interpretation for future studies. Following Nagali [29], if we require that at least 95 % of the area under the line shape be accurately described by the impact approximation, the criterion that the impact approximation is valid is then given by

$$\frac{\Delta v_c}{2} \le 0.079 \Delta v_{\text{imp}} . \tag{33}$$

Here, Δv_c [cm^{-1}] is the collisional broadening fullwidth given by

$$\Delta v_c(T,C,P) = 2\tilde{\gamma}_J^0 P \quad , \tag{34}$$

where P [atm] is the total gas pressure. In a regime above the boundary defined by Eq. (33), a line shape may still be modeled by Voigt function, but a breakdown at the far wings will likely be observed.

The so-called line-mixing effects caused by the interaction between different transitions become important when the frequency separation of collisionally-coupled transitions, relative to consecutive rotational levels, is smaller than, or of the same magnitude as the collisional width [31]. That is, if neighboring, interacting transitions v_{k1} and v_{k2} are such that

$$\left| v_{k1} - v_{k2} \right| \leq \frac{\overline{\Delta v_c}}{2},$$ (35)

then line-mixing effects should be considered. Here, $\left| v_{k1} - v_{k2} \right|$ is the separation distance in frequency between the interacting transitions, and $\overline{\Delta v_c}$ is the averaged collisional fullwidth of the two different transitions of interest. Since we have to consider multiple lines in Raman spectra we used the averaged line separation, $\overline{\left| v_{k1} - v_{k2} \right|} \equiv v_{sep}$ between each consecutive rotational/rovibrational line for practical convenience. Thus, the boundary of the line-mixing can be written as

$$v_{sep} \leq \frac{\overline{\Delta v_c}}{2}.$$ (36)

Here, values for v_{sep} were found to be 200.0, 19.8, 3.6, and 0.73 cm^{-1} for the *rot*-H_2 ($J = 0$ to 10), *vib*-H_2 ($J = 0$ to 17 in vibrational 1-0 transition), H_2O (000-100 transition), and N_2 (*Q*-branch, $J = 1$ to 40 in vibrational 1-0 transition), respectively.

Because of interrupted motions caused by the collisional scattering of molecules, a velocity-changing collision results in a line shape with a sub-Doppler linewidth, which involves line-narrowing effects [26]. If velocity-perturbing collisions are assumed to be

independent of state-perturbing collisions, then the Galatry profile ("soft" collision model) can be used to model the motional narrowing [29]. When the relationship given by

$$\Delta v_c \geq \Delta v_D \,, \tag{37}$$

is true, here Δv_D [cm^{-1}] is the full-width-half-maximum (FWHM) Doppler width, collisional broadening effects dominate the Doppler broadening so that the refinement of the motional narrowing effect is not necessary [29]. This is the third criterion for the line-shape model. Here, the Doppler width is given by

$$\Delta v_D(T) = \frac{2v_0}{c} \sqrt{2\ln(2)kT/M} \,, \tag{38}$$

where v_0 is the transition center frequency. Note that the motional narrowing is different from the collisional narrowing in its overall shape due to the line-mixing effect at high pressure.

From Eqs. (29-34 & 36-38), the following three boundaries are formed and they provide a way to choose the appropriate line-shape model for H_2, N_2, and H_2O gases over a range of pressure, temperature, and species concentration:

$$P = \frac{\Delta v_D/2}{\tilde{\gamma}_J^0(C,T)} : \text{ Galatry boundary} - A \tag{39}$$

$$P = \frac{0.079\Delta v_{imp}}{\tilde{\gamma}_J^0(C,T)} : \text{ Voigt boundary} - B \tag{40}$$

$$P = \frac{v_{sep}}{\tilde{\gamma}_J^0(C,T)} : \text{ Line-mixing boundary } - C \tag{41}$$

With these boundaries, the region with $P\tilde{\gamma}_J^0 \leq \Delta v_D/2$ indicates the neccesity of considering the motional narrowing effect, i.e. use of the Galatry profile; that with $\Delta v_D/2 < P\tilde{\gamma}_J^0 \leq 0.079\Delta v_{imp}$ indicates the use of the Voigt profile for entire line (additive approximation is valid); that with $0.079\Delta v_{imp} < P\tilde{\gamma}_J^0 < v_{sep}$ supports the use of the Voigt profile, with the caveat, that there is a possible breakdown in the far-wing (additive approximation is likely valid); and that with $P\tilde{\gamma}_J^0 \geq v_{sep}$ indicates the neccesity of considering the line mixing effect.

2-3. Target Flames

In order to analyze spectral interference in Raman scattering in high-pressure combustion environments, we generate thermodynamic properties for five different flames under the assumption of complete combustion and chemical equilibrium. Chemical equilibrium compositions of several different hydrogen-air flames, which hereafter we call "target flames", were then calculated by the CEA code [32] for assigned equivalence ratios, pressure (30 atm), and an initial gas temperature (300 K). Table 1 shows the calculated mole fractions of H_2, N_2, and H_2O and the adiabatic temperatures. The equivalence ratios were varied from 1.5 to 5.0, with the resulting temperatures varying from 1402 K to 2262 K. First, the calculated temperatures, pressure, and N_2 mole fractions as perturber concentrations were used as input parameters to calculate the collisional broadening coefficients and the line-shape diagrams. The calculated temperatures, pressure, and number densities of H_2, N_2, and H_2O (derived from the mole fractions and temperatures) were then used for the Raman spectral simulations.

3. Results and Discussion

3-1. Choice of Line-Shape

To choose the best line-shape function to model Raman spectra in our target flames over a range of pressure, temperature, and perturber concentration we introduce a three-dimensional diagram that is consists of the boundaries defined in Section 2-2. Figure 1 shows the diagram designed for the $S(3)$ line of the pure rotational H_2 (hereafter indicated *rot*-H_2) spectrum ($v_0 = 1035$ cm^{-1}). This diagram directs one to choose an appropriate line-shape model for spontaneous Raman spectra simulation in any flame of interest with a prior knowledge of pressure, temperature, and N_2 concentration. The locations of the five target flames (labeled case # 1 to # 5 in Table 1) are marked in the diagram to determine which line-shape model is the most appropriate. All five cases here are between boundary A and B as shown in Fig. 1, which indicates the entire line shape can be modeled by the Voigt profile with the additive approximation. Note that the same is true for other major *rot*-H_2 lines of higher J number while the Galatry boundary (boundary A) slightly moves toward higher pressure depending on the transition center frequency v_0.

Figure 2 shows a three-dimensional diagram for the rovibrational H_2 (hereafter indicated as *vib*-H_2) spectrum with points representing the target flames. Here the fundamental frequency of the *vib*-H_2 spectrum (4160 cm^{-1}) was assigned for the value of v_0 in the calculation of the diagram. In this figure, the line-mixing boundary (boundary C) appears because the averaged line separation (v_{sep}) of the *vib*-H_2 spectrum is 19.8 cm^{-1}, which is much smaller than rotational separation of the *rot*-H_2 spectrum by 180 cm^{-1}. All the target flames in Fig. 2 are also between boundary A and B, the Voigt profile regime.

Figure 3a and 3b show the line-shape diagrams for the vibrational Q-branches of N_2 and H_2O spectra with points representing the target flames. The fundamental vibrational Raman frequencies of N_2 and H_2O (2331 and 3657 cm^{-1}, respectively) were assigned to v_0 in the calculations of the diagrams. Here, only the self-broadening is considered for N_2, and the N_2 fraction relative to H_2O concentration is constant, i.e. $C = 0.65$. Accordingly, the diagrams have only two dimensions without a dimension of perturber N_2 concentration. As shown in Fig. 3a, all the target flames are located between boundary B and C, so the line shape for the N_2 Q-branch can be appropriately modeled by the Voigt function with the assumption of the additive approximation in the near-wing

region, but their line shape could break down in the far-wing regions. The impact and additive approximation are, for the most part, appropriate for the entire region of the H_2O spectrum in the target flames according to Fig. 3b.

In general, the Voigt profile was found to be a reasonable model for simulating the Raman spectrum over the range of pressure up to 30 atm, and for temperatures from approximately 1500 K to 2500 K. While there may be a slight effect of breakdown at the far wings of the N_2 Q-branch, the effect is small and is ignored in favor of the simplicity of using the Voigt function for the entire region of interest. This consequence is very useful for reducing the computational requirements of the spectral simulation and analysis. Hence, we used the Voigt profile for modeling the line shape of Raman spectra in the target flames. In the sections below, we will empirically validate the use of the Voigt profile for simulating Raman scattering spectra via comparisons between calculated spectra and experimental data.

In calculations of the Voigt-function a and x parameter [33] we used the overall convolution Gaussian width, Δv_G [cm^{-1}] given by

$$\Delta v_G(v, J) = \sqrt{\Delta v_D^2 + \Delta v_{spec}^2} . \tag{42}$$

Here Δv_{spec} is the instrumental function, which is the spectral resolution of a spectrograph. Finally, the profile of the Raman spectrum at temperature (T), and pressure (P) was calculated by the integration (via summation) of all Voigt-shaped lines based on the additive approximation assumption.

Regarding the temperature dependence of the collisional broadening coefficient there are at least two alternative expressions (CARS-, or HITRAN-expression) as we discussed above. We are not aware of a published report that indicates whether or not these two expressions make any difference to the line-shape diagram. In Fig. 4, we compare the line-shape diagrams derived from the two different expressions for the broadening coefficient. As shown in Fig. 4, the boundary A, and B based on the two expressions, which have been validated by the different spectroscopic experiments and calculations, agree very well when the HITRAN-based temperature dependence coefficient, n was set

to 0.15. This agreement indicates the both expressions are comparable, and that they can be applied to spontaneous Raman scattering applications, even though we used a CARS-derived expression for H_2, and a HITRAN-derived expression for N_2, and H_2O in this paper.

3-2. Validation of the Raman Model

We validate our theoretical models for the Raman scattering intensity and line shapes in high-pressure environments by comparison with experimental data measured in high-pressure flames. We used a specially designed high-pressure gaseous burner that provides a precise and stable source of hot combustion products in a high-pressure environment. The burner provides a homogeneous stream of combustion products via a tightly-spaced array of multiple fuel-rich H_2–air premixed flamelets (10 atm). In this particular premixed burner design, the 7 x 7 array of premixed flame tubes (1.1 mm dia.) had a center-to-center spacing of 2.60 mm. Spontaneous Raman scattering from H_2, N_2, and H_2O were then measured at a reduced-temperature, post-flame zone using our SRS diagnostic system which consists of a pulsed Nd:YAG laser, a laser pulse-stretcher, a high-speed electro-mechanical shutter, and a spectrometer fitted with a non-image-intensified CCD camera. For the simulations, we used an instrumental resolution of ν_{spec} = 35 cm^{-1} which corresponds to the spectral resolution of the spectrometer used in the measurement. It should be noted that our previous measurements with this high-pressure burner indicated that a condition close to the chemical equilibrium was reached over the range of equivalence ratio at the measurement location, however, the measured temperatures were below the adiabatic equilibrium temperatures by more than 100 K [34]. Further details on the burner and diagnostics have been described in our previous reports [25, 34-35].

For a quantitative simulation of a Raman spectrum, we empirically determine the factor $(\alpha'/\beta')^2$, the squared ratio of the isotropic term to the anisotropic term of the polarizability derivative, and we verify the relative intensity of the Q-branch to the S/O-branches in vibrational N_2 or H_2 Raman spectrum. Note that calculated S-/O-branches of N_2, or H_2 Raman spectrum using theoretically determined values of α' and β' [16-17] do

not agree with our experimental data, thus we determined these values empirically as follows. We measured the factor $(\alpha'/\beta')^2$ for N_2, or H_2 vibrational Raman spectrum in ambient-temperature air and compare it with a calculated spectrum at the same condition. As shown in Fig. 5, we found the best agreement in terms of the relative intensity of the Q-branch to the O-, and S-branch between data for the room air and a calculated N_2 Raman spectrum at 300 K when using the factor for $(\alpha'/\beta')^2$ set at a value of 0.25. The suitability of this value for N_2 was also substantiated by the good agreement between measured data and calculated values for a N_2 Raman spectrum in a 10-atm H_2–air flames ($\phi = 2.06$) as shown in Fig. 6. We found that the factor $(\alpha'/\beta')^2$ for H_2, when set at 0.35, provided the best agreement between a calculated O-branch intensity of the vib-H_2 spectrum and a measured spectrum from a 10-atm H_2–air flame ($\phi = 3.0$) as shown in Fig. 7.

We then compare the experimental Raman spectra measured in 10-atm fuel-rich H_2–air flames with theoretical Raman spectra calculated at the temperatures determined experimentally by the line-intensity distribution of the rot-H_2 Raman spectrum [13,25]. Figure 6 shows the measured ($\phi = 2.06$) and calculated (T = 1425 K) results of the rot-H_2 and the vibrational N_2 Raman spectra. The transition frequencies (wavelength) and line shapes of calculated spectra show excellent agreement with experimental data for both species. As indicated in this Fig. 6, the N_2 O-branch is a possible spectral interference (cross-talk) with the $S(9)$ and $S(8)$ lines of the rot-H_2 band. Also, the rot-H_2 $S(10)$ line, which is barely seen in this figure, is completely overwhelmed by the N_2 Q-branch. We will examine these spectral interferences in detail in the section below.

Figure 7 shows the measured ($\phi = 3.0$) and calculated (T = 1133 K) results of the vibrational H_2O and the vib-H_2 Raman spectra. The calculated spectra for both species show excellent agreement with the experimental data in terms of the transition frequency, intensity and line shape. Note that we can clearly observe the spectral interference between the H_2O spectrum and the vib-H_2 $O(0,3)$ line around 657 nm. This interference is important because it affects the determination of the H_2O number density in fuel-rich high-pressure flames, thus we will examine it in detail in the following section.

Based on the comparisons between the spectral simulation and the experimental data, we have shown that the current theoretical models for Raman scattering line position,

intensity, and shape, are of sufficient accuracy to examine the effects of Raman spectral interferences amongst the major species of interest in high-pressure H_2-air flames.

Quantitative Comparison between Different Species

In order to quantitatively analyze the contribution of spectral interferences in the overall Raman spectra for all species of interest, the relative scattering intensities of each different species has to be realized and properly implemented in the calculations. To do this, we define an empirical scaling factor for the scattering intensity of a rotational or vibrational Raman spectrum of species j relative to the N_2 Raman scattering intensity as follows:

$$\Gamma_j = \frac{\sum_{n=a}^{b} {}^{ms}I_j^{\phi,P} \Big/ N_j(\phi,P,T_{ms})}{\sum_{n=c}^{d} {}^{ms}I_{N2}^{\phi,P} \Big/ N_{N2}(\phi,P,T_{ms})}, \tag{43}$$

where ${}^{ms}I_j^{\phi,P}$ is the pixel intensity (CCD count per pixel) of a measured rotational or vibrational Raman spectrum of species j at equivalent ratio of ϕ and pressure of P; n is the pixel number and a, b, c, or d indicate a corresponding pixel range for the summation of the spectrum of species j; $N_j(\phi,P,T_{ms})$ is the calculated chemical-equilibrium number density of species j for ϕ, P, and the measured temperature T_{ms} via the *rot*-H_2 spectrum. The subscript, 'N2' indicates the molecular nitrogen species used as the reference.

Based on the scaling factor Γ_j and the intensity-normalized calculated Raman spectrum, the scale-corrected intensity of a theoretical Raman spectrum for species j at pressure of P and temperature of T can be obtained by

$$^{cal}I_j'(P,T) = \Gamma_j N_j(\phi,P) \frac{^{cal}I_j(P,T)}{\int {}^{cal}I_j(P,T)d\lambda}, \tag{44}$$

where $N_j(\phi, P)$ is the adiabatic number density of species j for ϕ and P; and $^{cal}I_j(P,T)$ is the intensity of the calculated Raman spectrum at P and T.

Based on Eq. (43) and the measured Raman scattering data obtained in 10-atm H_2–air flames (Fig. 6, and Fig. 7), we were then able to determine the scaling factor for each species. Note that the instrumental function did not affect the resulting scale-corrected spectra, since the spectral intensity response of the entire optical system used for the measurements are calibrated in both intensity and wavelength using standard reference lamps. We then make the assumption that the combustion products have reached chemical equilibrium, and also with use of the scaling factors described above, and by using the parameters found in Table 1, we calculate the scale-corrected rotational or vibrational Raman spectra of N_2, H_2, and H_2O in 30-atm fuel-rich H_2–air flames. This finally enables a quantitative comparison of the spectral interferences between the different species of interest.

3-3. Spectral Interference

According to the experimental data shown in Figs. 6 and 7, there are two kinds of noticeable spectral interferences in Raman scattering in fuel-rich hydrogen flames: interference between the higher J-number ($8 \leq J \leq 11$) *rot*-H_2 lines and the N_2 spectrum; and between the *vib*-H_2 $O(0,3)$ line and the vibrational H_2O spectrum. The behavior of Raman spectral interference is typically nonlinear since the rate of spectral interference is a function of both temperature and number density of at least two species in a spectral range of interest. For instance, in fuel-*rich* flames, rotational H_2 line intensities of transitions with higher J states are determined by a trade-off between the Boltzmann rotational distribution and the number density which is governed by the local stoichiometry. Thus, one of our questions is in which case does the Raman interference become more important: H_2-rich, lower-temperature flames, or nearly stoichiometric, higher-temperature flames? In order to examine this question in a quantitative fashion, we simulated rotational and/or vibrational Raman spectra of H_2, N_2, and H_2O in high-pressure hydrogen-air flames at different equivalence ratios using the theoretical formalism presented above.

Interference between rot-H$_2$ and vib-N$_2$

Figure 8 shows the calculated Raman spectra of the *rot*-H$_2$ *S*-branch and the vibrational N$_2$ spectra in 30-atm H$_2$–air flames from $\phi = 1.5$ to 5.0. Occurrences of spectral interference among these spectra can be clearly seen in this series of spectral simulations. Our simulation indicates that it is particularly important to quantitatively analyze the interference that the *rot*-H$_2$ *S*(10) line gives to the N$_2$ *Q*-branch since the *S*(10) line is completely overlapped by the N$_2$ line. Figure 8 also confirms that there is an interference between the N$_2$ *O*-branch (the blue-side tail) and the lines from the *rot*-H$_2$ *S*(8), or *S*(9) lines; and that there is an interference between the N$_2$ *S*-branch (the red-side tail) and the *rot*-H$_2$ *S*(11) line. Note that the higher *J*-number ($\geq$ 9) line intensities of the *rot*-H$_2$ do not necessarily become stronger with increase of the equivalence ratio, while the lower *J*-number ($\leq$ 7) line intensities apparently increase with the equivalence ratio. The interference between the *rot*-H$_2$ and the N$_2$ spectrum indicates that further attention should be paid to the spectral shape of the N$_2$ *Q*-branch in hydrogen-rich environments. This effect is further exacerbated by the fact that the N$_2$ *Q*-branch gradually shrinks as temperature lowers due to the less population of higher vibrational states.

In order to quantify and clarify the flame conditions in which the interference is significant, we define the cross-talk rate as the overlap rate between one spectrum and another. The cross-talk rate, K_r is the ratio of the integrated spectral area of one spectrum (always smaller one) to that of another spectrum, which interferes with the former spectrum, for a certain range of wavelength. The spectral range of the integration for each case is shown in the figure captions. Figure 9 shows the cross-talk rate between the N$_2$ *O*-branch and the *rot*-H$_2$ *S*(8) line (hereafter indicated as $K_r^{\text{N-Hs8}}$); that between the N$_2$ *O*-branch and the *rot*-H$_2$ *S*(9) line (indicated as $K_r^{\text{N-Hs9}}$); and that between the *rot*-H$_2$ *S*(10) line and the N$_2$ *Q*-branch (indicated as $K_r^{\text{Hs10-N}}$) over the range of equivalence ratios used in this study. A high amount of the cross-talk, $K_r^{\text{N-Hs8}} = 0.48$ (48% overlap within the spectral range) is observed at $\phi = 1.5$. $K_r^{\text{N-Hs8}}$ becomes smaller as ϕ increases, yet $K_r^{\text{N-Hs8}}$ is more than 0.08 for ϕ over 4.0. Similarly, the cross-talk $K_r^{\text{N-Hs9}}$ reaches more than 0.65 (65% overlap) at $\phi = 1.5$. The higher amount of cross-talk arising from the "hot bands"

of the N_2 Q-branch also contributes to the interference. K_r^{N-Hs9} has a minimum value of 0.3 (30% overlap) at $\phi = 3.0$ and stays over this value over the range of ϕ examined here. It is evident from Fig. 9 that the $S(8)$ and $S(9)$ lines should not be included in the temperature determination process via the *rot*-H_2 distribution in fuel-rich flames because of the higher level of interference.

In Fig. 9, the cross-talk rate K_r^{N-Hs10} shows a different behavior than the previous cases for the $S(8)$ and $S(9)$ lines: it varies from 0.023 (2.3% overlap) to its maximum value around 0.036 (3.6% overlap) at $\phi \sim 2.5$. A cross-talk level of several percent is not insignificant, and may affect the accurate measurement of N_2 number density and/or N_2 vibrational temperature, if this effect is not accounted for in the subsequent analysis.

As an aid in the interpretation of Raman spectra with such an interference, we propose a practical method to compensate the cross-talk effect of K_r^{N-Hs10} using a theoretical calculation with a priori knowledge of the temperature and an observed *rot*-H_2 line intensity data. Since the intensity distribution of the *rot*-H_2 Raman transitions is governed only by temperature under assumption of the thermal equilibrium, the relative intensity ratio of any pair of lines in the *rot*-H_2 Raman spectrum can be theoretically derived based on a known temperature. Hence one can estimate the line intensity of the *rot*-H_2 $S(10)$ from a measured intensity of, for instance, the *rot*-H_2 $S(6)$ line, which is generally strong enough to be measured from background noise and free from any major spectral inference. The theoretical Raman intensity ratio of the *rot*-H_2 $S(10)$ line to the $S(6)$ line, R_{rH}^{s10-s6}, was calculated with Eq. (21) over a range of temperature. The polynominal coefficients of the curve fitted to the theoretical plots of R_{rH}^{s10-s6} are shown in Table 2. The thermodynamic temperature can be measured by the intensity distribution of the *rot*-H_2 Raman spectrum [13] within a few percent accuracy [25] and thus, a corresponding intensity ratio between the two lines at the temperature can be obtained via the polynominal function in Table 2. The "hidden" contribution of the *rot*-H_2 $S(10)$ to the N_2 Q-branch would be then revealed by multiplying the obtained intensity ratio to the measured the $S(6)$ line intensity in a Raman spectrum of interest. Finally, the obtained $S(10)$ line intensity would then be subtracted from a integrated intensity of the N_2 spectrum to find a corrected N_2 number density.

Note that the *rot*-H_2 S(7) shown in Fig. 8 is not suitable for use in this cross-talk compensation process because it coincides with the common atomic Na emission line (3s–3p transition) near 589 nm, which can be quite intense in industrial flames. For the other important cross-talk contributors to the vibrational N_2 spectrum resulting from the S(9), or S(11) lines in H_2, a cross-talk calibration matrix formalism as previously mentioned in the Introduction section would have to be implemented in order to compensate for these effects.

Interference between vib-H₂ and vib-H₂O

Figure 10 shows the calculated vibrational Raman spectra of H_2 and H_2O in 30-atm H_2–air flames over the range of equivalence ratio ranging from 1.5 to 5.0. As the equivalence ratio increases (thus, the number density of hydrogen molecule increases), the intensity of the *vib*-H_2 spectrum becomes stronger while the intensity of the H_2O spectrum do not change much. As clearly seen in Fig. 11, the *vib*-H_2 O(0,3) line significantly interferes with H_2O, particularly in highly H_2-rich flames. There is also interference around 661 nm by higher rovibrational transitions of the *vib*-H_2 Q-branch. In order to clarify these interferences, we obtain the cross-talk rate between the *vib*-H_2 and the H_2O spectra ($K_r^{\text{vH-W}}$) following the above-mentioned manner. The result over the range of equivalence ratios is shown in Fig. 11. The curve in Fig. 11 indicates that the cross-talk rate $K_r^{\text{vH-W}}$ has a monotonic and positive relation with equivalence ratio. Notice that the cross-talk rate $K_r^{\text{vH-W}}$ has a value of 0.08 (8% overlap) at $\phi = 1.5$ and reaches 0.18 (18% overlap) at $\phi = 5.0$. This level of cross-talk causes major errors in the measurement of H_2O number density if not properly accounted for.

Since the *vib*-H_2 O(0,3) line are mostly overwhelmed by the stronger H_2O spectrum, it is generally hard to realize this interference. We then propose the same analytical compensation technique previously used for the cross-talk rate $K_r^{\text{N-Hs}}$[10] to remove the contribution by the *vib*-H_2 O(0,3) line to the H_2O spectrum. Using the a priori knowledge of temperature determined by the *rot*-H_2 Raman transitions and a measured *vib*-H_2 line intensity, a corresponding *vib*-H_2 O(0,3) line intensity can be obtained and subtracted from the H_2O spectral intensity data. Here, we suggest use of the *vib*-H_2 O(0,5) line for

the compensation process because it is the strongest line amongst the vib-H_2 O-branches and is relatively free from major spectral inferences. The theoretical Raman intensity ratio of the vib-H_2 $O(0,3)$ line to the $O(0,5)$ line, R_{vH}^{o3-o5}, was calculated over a range of temperature. The polynominal coefficient of the fitting curve to the theoretical plots of R_{vH}^{o3-o5} is shown in Table 2. The value calculated from the polynominal function in Table 2 with a known temperature and a vib-H_2 $O(0,5)$ intensity can serve to compensate the H_2O spectral intensity in fuel-rich flames.

Another source of interference that arises from the blue-side tail of the vib-H_2 Q-branch around 661 nm, can cause a minor overestimation in measurements of H_2O number density by less than ~1.5% (e.g. at $\phi = 5.0$) after compensating for the vib-H_2 $O(0,3)$ contribution. There is not a simple, straightforward analytical expression for this interference because this portion of the vib-H_2 Q-branch contains multiple lines that originate from different rovibrational transitions, and its dependence on the spectral band factor (spectral resolution and/or pressure broadening) is complicated. Thus, the cross-talk matrix calibration method needs to be applied to take this interference into account.

Temperature dependence of spectral interferences

It is well known that the off-diagonal terms of the cross-talk calibration matrix represent spectral interference of one species onto another and may be expressed as a function of temperature [2-3,6-7]. Although the temperature dependence of the cross-talk matrix has been typically assumed to be a polynomial relation [6-7], we are not aware of any studies that can substantiate this common assumption for high-pressure combustion environments. Figure 12 shows the cross-talk rate normalized by the number density of hydrogen (K_r / N_{H2}) as a function of temperature regarding the N_2 Q-branch and H_2O Raman spectra. By normalizing by the number density of H_2, which is the only species whose Raman spectrum (either rotational or vibrational) interferes with the N_2 or H_2O Raman spectrum in H_2-Air flames, a pure dependence of the cross-talk on temperature can be extracted. From Fig. 12 we confirm that the temperature dependence of the H_2-normalized cross-talk for nitrogen and water is well approximated by a monotonic, second-order (or less) polynomial function for the hydrogen flames in this study.

Note that the spectral database for the H_2O Raman scattering used here does not include a treatment of the hot bands, which is significant on the blue-side of the H_2O spectrum above a temperature of 2000 K. As a result, the database tends to underestimate the spectral intensity by no less than 10% in high temperature regions. Thus, we have to be aware that an experimentally observed H_2O Raman spectrum will be more spread out towards the blue-side than predicted by our calculation. This hot-band behavior of H_2O could interfere with the *vib*-H_2 $O(0,4)$ line in the equivalence ratio range from about $1.0 < \phi < 2.0$, in high-temperature flames. According to our experimental data (with the same spectral resolution of the present simulation) in 10-atm H_2–air flames over the wide range of equivalence ratio ($\phi = 0.2 - 5.0$) [34], the blue-side tail end of H_2O spectrum touches the *vib*-H_2 $O(0,4)$ line but barely interferes even at $\phi = 1.5$. Hence it is not necessary to include the *vib*-H_2 $O(0,4)$ in the cross-talk calibration process for H_2O Raman spectrum.

4. Conclusions

In order to improve and make spontaneous Raman scattering diagnostics more quantitative and accurate for the measurement of temperature and species in high-pressure combustion, we theoretically investigated the spectral interference of Raman spectra in fuel-rich, H_2–air flames at pressures up to 30 atm. The rotational/vibrational Raman scattering of H_2, N_2, and H_2O were modeled with particular attention paid to the O-/S-branches as well as the common Q-branch using an anharmonic oscillator model and the most recent spectral database available in literature. We applied an analytical methodology, which is based on a collision-scale analysis and molecular vibration, to validate an appropriate line-shape model for simulating the Raman spectrum in high-pressure flames. The line-shape diagrams for the species showed that the use of the Voigt profile with the additive approximation was appropriate and practical for the Raman spectral analysis at the target flame conditions used in this study.

Our model was validated by direct comparisons between the calculated Raman spectra and measured data in 10-atm H_2–air fuel-rich flames, which showed excellent agreement in every detail, including the O-, and S-branch intensities. The spectral

interferences amongst the Raman spectra of the species of interest were then calculated for the target high-pressure H_2–air flames, and were analyzed over the range an equivalence ratio range of $\phi = 1.5$ to 5.0, and temperature. Below is a summary of the findings of the quantitative analysis on the Raman spectral interference in 30-atm fuel-rich H_2–air flames:

(i)   The spectral overlap (cross-talk rate) between the pure rotational H_2 $S(8)$ line and the N_2 O-branch was as high as 48% at $\phi = 1.5$.

(ii) The spectral overlap between the pure rotational H_2 $S(9)$ line and the N_2 O-branch was 65% at $\phi = 1.5$ and about 30% at $\phi = 3.0$.

(iii) The spectral overlap between the pure rotational H_2 $S(10)$ line and the N_2 Q-branch was 3.6% at $\phi \sim 2.5$.

(iv) The spectral overlap between the vibrational H_2 $O(0,3)$ line and the H_2O spectrum was 18% at $\phi = 5.0$.

In addition, we introduce an analytical technique using the Raman intensity ratio for a neighboring pair of the H_2 lines, to compensate for the cross-talk between the *rot*-H_2 $S(10)$ line and the N_2 Q-branch; and that between the *vib*-H_2 $O(0,3)$ line and the H_2O spectrum. We also provide numerical coefficients for implementing this compensation technique. Finally, we demonstrated that the Raman cross-talk between *rot*-H_2 and N_2, or *vib*-H_2 and H_2O has a second-order (or less) polynomial relation with flame temperature; this information can then be used as an aid in selecting an appropriate functional form for calibrations in future studies.

Since the collisional broadening effects on spectral line-shape are relatively minor at the modest spectral resolution considered here, the findings and techniques discussed in this report are applicable to both atmospheric and high-pressure (at least up to 30 bar) flames.

Acknowledgement

authors (J.K.) held a National Research Council Research Associateship Award at NASA GRC.

References

(1) A.C. Eckbreth, *Laser Diagnostics for Combustion Temperature and Species*: 2nd Ed., Gordon and Breach Publishers, The Netherlands, 209-273 (1996).

(2) E. P. Hassel, and S. Linow, "Laser Diagnostics for Studies of Turbulent Combustion," *Meas. Sci. Technol.* **11**, R37-R57, (2000).

(3) P. A. Nooren, M. Versluis, T. H. van der Meer, R. S. Barlow, J. H. Frank, "Raman-Rayleigh-LIF measurements of temperature and species concentrations in the Delft piloted turbulent jet diffusion flame," *Appl. Phys. B* **71**, 95-111 (2000).

(4) Y. Gu, Y. Zhou, H. Tang, E. W. Rothe, and G. P. Reck, "Presure Dependence of Vibrational Raman Scattering of Narrow-Band, 248-nm, Laser Light by H_2, N_2, O_2, CO_2, CH_4, C_2H_6, and C_3H_8 as High as 97 bar," *Appl. Phys. B* **71**, 865-871 (2000).

(5) T. S. Cheng, T. Yuan, C.-C. Lu, and Y.-C. Chao, "The Application of Spontaneous Vibration Raman Scattering for Temperature Measurements in High Pressure Laminar Flames," *Combust. Sci. Technol.* **174**, 111-128 (2002).

(6) A. R. Masri, R. W. Dibble, R. S. Barlow, "The Structure of Turbulent Nonpremixed Flames Revealed by Raman-Rayleigh-LIF Measurements," *Prog. Energy Combust. Sci.* **22**, 307-362 (1996).

(7) Q. V. Nguyen, R. W. Dibble, C. D. Carter, G. J. Fiechtner and R. S. Barlow, "Raman-LIF Measurements of Temperature, Major Species, OH, and NO in a Methane-Air Bunsen Flame," *Combust. Flame* **105**, 499-510 (1996).

(8) M. S. Mansour, and Y.-C. Chen, "Line-Raman, Rayleigh, and Laser-Induced Predissociation Fluorescence Technique for Combustion with a Tunable KrF Excimer Laser," *Appl. Opt.* **35**:21, 4252-4260 (1996).

(9) M. Lapp, "Flame temperatures from vibrational Raman scattering," in *Laser Raman Gas Diagnostics*, M. Lapp, and C. M. Penny, eds. (Plenum, New York), 107-145 (1974).

(10) E. P. Hassel, "Ultraviolet Raman-scattering measurements in flames by the use of a narrow-band XeCl Excimer lsaser," *Appl. Opt.* **32**, 4058-4065 (1993).

(11) A. Lévy, N. Lacome, and C. Chackerian, "Collisional Line Mixing": in *Spectroscopy of the Earth's Atmosphere and Interstellar Medium*, K. N. Rao, and A. Weber, eds. (Academic Press, San Diego), 261-422, (1992); and references therein.

(12) D. A. Long, *Raman Spectroscopy*, McGraw-Hill, London, CRS1-16, (1977).

(13) M. C. Drake, and G. M. Rosenblatt, "Rotational Raman Scattering from Premixed and Diffusion Flames," *Combust. Flame* **33**, 179-196, (1978).

(14) G. Hertzberg, *Molecular Spectra and Molecular Structure - I. Spectra of Diatomic Molecules*: 2nd Ed., Krieger Publishing Company, Florida, 66-141, (1950).

(15) K. P. Huber, and G. Hertzberg, *Molecular Spectra and Molecular Structure - IV. Constants of Diatomic Molecules*, Van Nostrand Reinhold Company, New York, (1979). Electronic database might be available at http://webbook.nist.gov/chemistry/ (NIST standard reference database – Chemistry WebBook).

(16) W. Knippers, K. van hel Voort, and S. Stolte, "Vibrational Overtones of the Homonuclear Diatomics (N_2, O_2, D_2) Observed by the Spontaneous Raman Effects," *Chem. Phys. Let.* **121**, 279-286, (1985).

(17) D. M. Bishop, and J. Pipin, "Calculated Raman Overtone Intensities for H_2 and D_2," *J. Chem. Phys.* **94**, 6073-6080, (1991).

(18) L. S. Rothman, C. P. Rinsland, A. Goldman, S. T. Massie, D. P. Edwards, J.-M. Flaud, A. Perrin, C. Camy-Peyret, V. Dana, J.-Y. Mandin, J. Schroeder, A. McCann, R. R. Gamache, R. B. Wattson, K. Yoshino, K. V. Chance, K.W. Jucks, L.R. Brown, V. Nemtchinov, and P. Varanasi, "The HITRAN Molecular Spectroscopic Database and HAWKS (HITRAN Atmospheric Workstation): 1996 Edition," *J. Quant. Spectrosc. Radiat. Transfer* **60**, 665-710 (1998).

(19) J. M. Flaud, C. Camy-Peyret, "Vibration-Rotation Intensities in H_2O-Type Molecules Application to the $2v_2$, v_1 and v_3 Bands of $H_2^{16}O$," *J. Mol. Spectrosc.* **55**, 278-310 (1975).

(20) G. Avila, J. M. Fernández, B. Maté, G. Tejeda, and S. Montero, "Ro-vibrational Raman Cross Sections of Water Vapor in the OH Stretching Region," *J. Mol. Spectrosc.* **196**, 77-92, (1999).

(21) R. R. Gamache, R. L. Hawkins, L. S. Rothman, Total Internal Partition Sums in the Temperature range 70-3000K: Atmospheric Linear Molecules," *J. Mol. Spectrosc.* **142**, 205-219, (1990).

(22) V. Bergmann, W. Stricker, "H_2 CARS thermometry in a fuel-rich, premixed, laminar CH_4/air flame in the pressure range between 5 and 40 bar," *Appl. Phys. B* **61**, 49-57 (1995).

(23) J. Hussong, W. Stricker, X. Bruet, P. Joubert, J. Bonammy, D. Robert, X. Michaut, T. Gabard, H. Berger, "Hydrogen CARS Thermometry in H_2-N_2 Mixtures at High Pressure and Medium Temperatures: Influenec of Linewidths Models," *Appl. Phys. B* **70**, 447-454 (2000).

(24) J. Hussong, R. Lückerath, W. Stricker, X. Bruet, P. Joubert, J. Bonammy, and D. Robert, "Hydrogen CARS Thermometry in High-Pressure H_2–air Flame. Test of H_2 Temperature Accuracy and Influence of Line Width by Comparison with N_2 CARS as Reference," *Appl. Phys. B* **73**, 165-172 (2001).

(25) J. Kojima, and Q. V. Nguyen, "Measurement and simulation of spontaneous Raman scattering in high-pressure fuel-rich H_2–air flames," *Meas. Sci. Technol.* **15**, 565-580 (2004).

(26) P. L. Varghese, R. K. Hanson, "Collisional Narrowing Effects on Spectral Line Shapes Measured at High Resolution," *Appl. Opt.* **23**, 2376-2385 (1984).

(27) A. P. Thorne, *Spectrophysics*, Chapman and Hall, London, (1974), 255-285.

(28) Th. Bouche, Th. Dreier, B. Lange, J. Wolfrum, E. U. Franck, W. Schilling, "Collisional Narrowing and Spectral Shift in Coherent Anti-Stokes Raman Spectra of Molecular Nitrogen up to 2500 bar and 700 K," *Appl. Phys. B* **50**, 527-533 (1990).

(29) V. Nagali, Ph.D. Dissertation, Mech. Eng. Dept., Stanford University, TSD report 117, 8-35 (1998).

(30) P. Atkins, *The Elements of Physical Chemistry* (2nd Ed.), W.H.Freeman and Company, New York, 19, (1996).

(31) J.-M. Hartmann, M. Y. Perrin, Q. Ma, R. H. Tipping, "The Infrared Continuum of Pure Water Vapor: Calculations and High-Temperature Measurements," *J. Quant. Spectrosc. Radiat. Transfer* **49**, 675-691 (1993).

(32) S. Gordon and B. J. McBride, "Computer Program for Calculation of Complex Chemical Equilibrium Compositions and Applications – I. Analysis," NASA RP-1311, (1994). http://www.lerc.nasa.gov/WWW/CEAWeb/xHowCEA.html.

(33) S. R. Drayson, "Rapid Computation of the Voigt Profile," *J. Quant. Spectrosc. Radiat. Transfer* **16**, 611-614, (1976).

(34) J. Kojima, and Q.-V. Nguyen, "Development of a High-Pressure Gaseous Burner for Calibrating Optical Diagnostic Techniques," NASA/TM 2003-212738, (2003). Available electronically at http://gltrs.grc.nasa.gov.

(35) J. Kojima, and Q. V. Nguyen, "Laser Pulse-Stretching Using Multiple Optical Ring-Cavities," *Appl. Opt.* **41**, 6360-6370, (2002).

Table 1 Adiabatic temperatures and species compositions calculated for hydrogen-air combustion system using the CEA chemical equilibrium code using assigned pressures and equivalence ratios.

Case #	1	2	3	4	5
P [atm]	30	30	30	30	30
ϕ	1.5	2.0	3.0	4.0	5.0
T [K]	2262	2065	1770	1560	1402
H_2 [Mole frac.]	0.147	0.257	0.409	0.509	0.58
H_2O [Mole frac.]	0.295	0.257	0.205	0.17	0.145
N_2 [Mole frac.]	0.55	0.479	0.381	0.317	0.271

Table 2 Polynomial coefficients of curves fitted to the theoretically calculated intensity ratios of lines for the rotational hydrogen *S*- branch and vibrational hydrogen *O*-branch as a function of temperature (K). The polynomial coefficients have the form of

$$R(T) = aT^4 + bT^3 + cT^2 + dT + e.$$

Coeff.	a	b	c	d	e
$R_{rH}^{s10\text{-}s6}$	...	$-1.813 \cdot 10^{-11}$	$1.362 \cdot 10^{-7}$	$-1.676 \cdot 10^{-4}$	$5.818 \cdot 10^{-2}$
$R_{vH}^{o3\text{-}o5}$	$4.089 \cdot 10^{-13}$	$-3.354 \cdot 10^{-9}$	$1.047 \cdot 10^{-5}$	$-1.508 \cdot 10^{-2}$	9.504
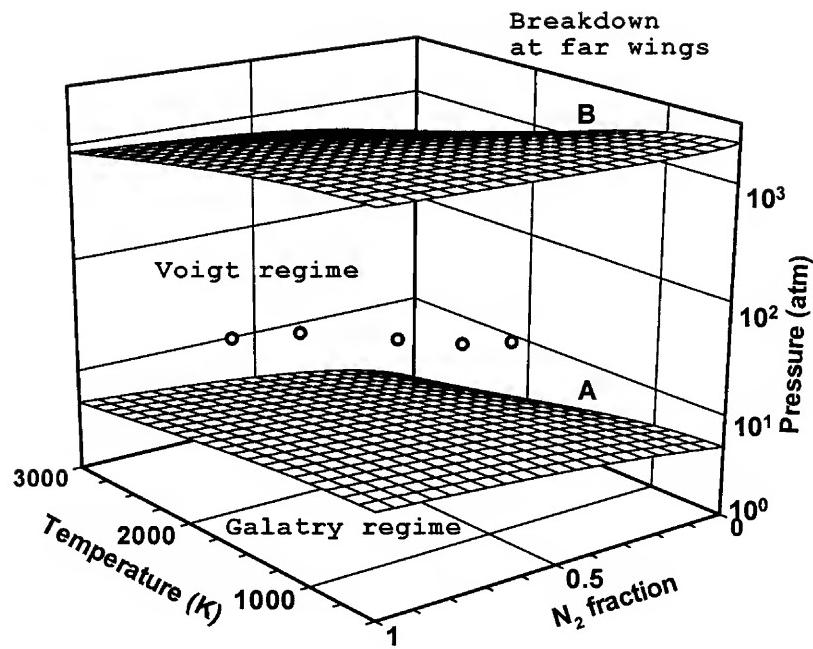
Fig. 1   Three-dimensional diagram used for choosing the proper line-shape
model in high-pressure combustion environments for the S(3) line of pure
rotational H_2 Raman spectrum.   Pressure is in log scale. White *circles*
indicate the locations of the five target flames in shown in Table 1.
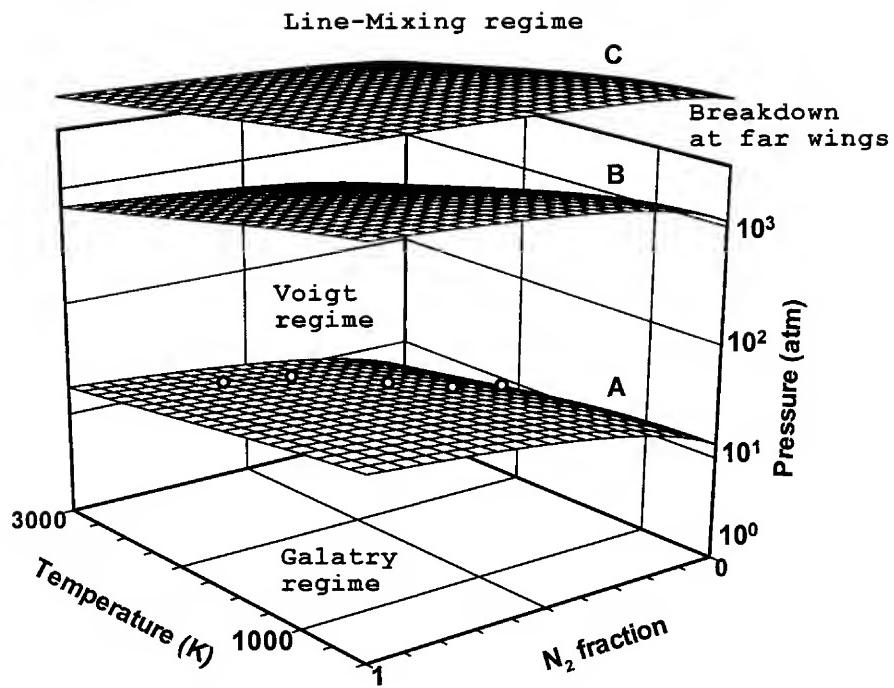
Fig. 2 Three-dimensional diagram used for choosing a proper line-shape model in high-pressure combustion environments for vibrational H_2 Raman spectrum. Pressure is in log scale. White *circles* indicate the locations of the five target flames shown in Table 1.

(a)
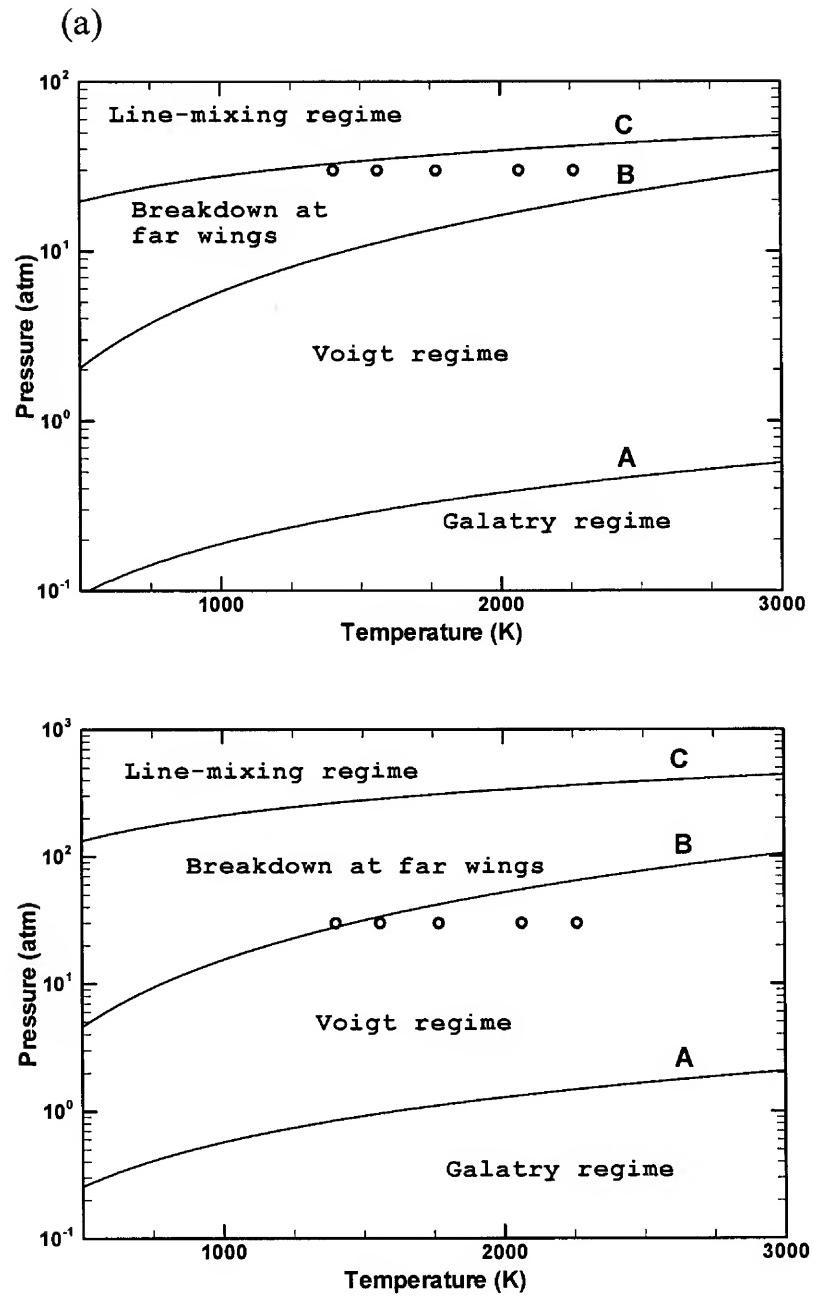
Fig. 3 Two-dimensional diagrams used for choosing a proper line-shape model in high-pressure combustion environments for (a) vibrational N_2 Raman Q-branch (self-broadening), and (b) vibrational H_2O Raman ($C = 0.65$). White *circles* indicate the locations of the five target flames shown in Table 1.
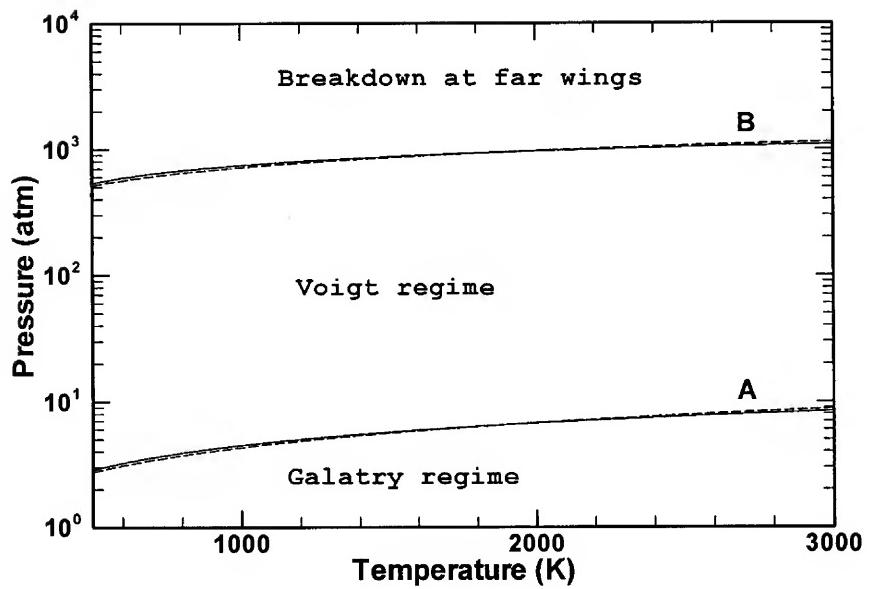
Fig. 4 Comparison of the boundaries in the diagram for the rotational H_2 $S(3)$ line with different pressure broadening coefficients based on the CARS-expression and the HITRAN-expression. *Solid line*: CARS-expression; *dashed line*: HITRAN-expression with temperature coefficient $n = 0.15$.
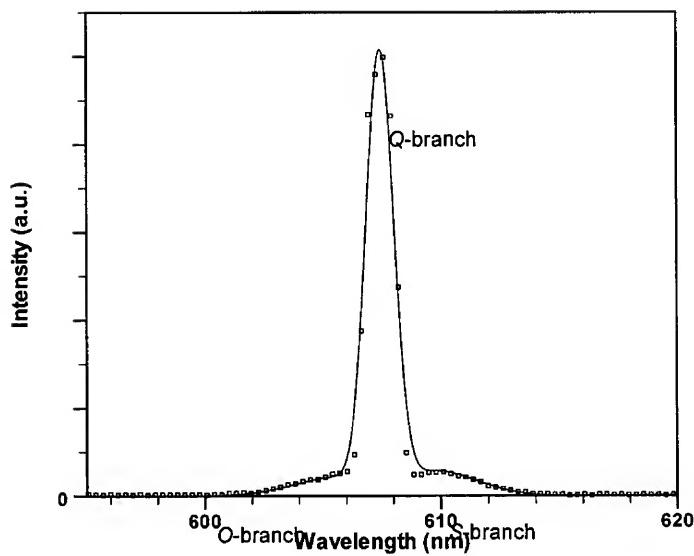
Fig. 5 Measured and calculated Raman spectra of vibrational N_2 in room-temperature air (300 K) at 10 atm used to determine the ratio of mean/anisotropic polarizability derivatives, α'/β' of nitrogen. Experiment (*points*): 200-shot averaged, 0.1 mm spectrometer slit. Calculation (*line*): ν_{spec} = 35 cm^{-1}.
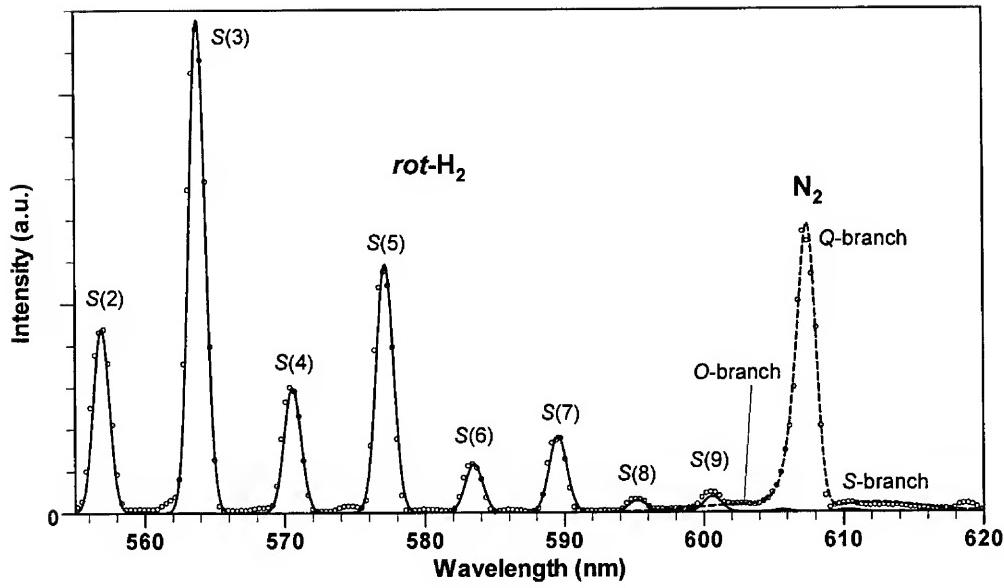
Fig. 6 Measured and calculated vibrational N_2 and rotational H_2 Raman spectra in a 10-atm H_2-air flame. The spectra were calculated using the experimentally determined temperature via the rot-H_2 transitions, and was found to be 1425 K (ν_{spec} = 35 cm^{-1}). The experimental data is represented by the *points* (ϕ= 2.06, 200-shot averaged, 0.1 mm spectrometer slit). *Solid line*: rotational H_2. *Dashed line*: vibrational N_2. Two calculated lines are shown separately but not superimposed.
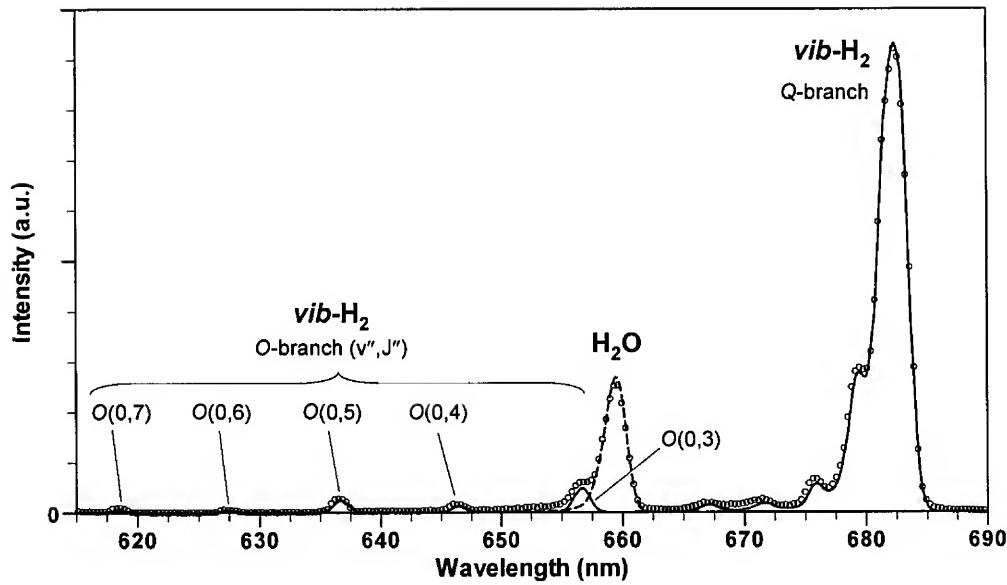
Fig. 7 Measured and calculated Raman spectra of H_2O, and vibrational H_2 in a 10-atm H_2-air flame. The spectra were calculated at an experimentally determined temperature obtained via the rot-H_2 transitions (not shown in this figure), and was found to be 1133 K (ν_{spec} = 35 cm^{-1}). The experimental data is represented by *points* (ϕ = 3.0, 200-shot averaged, 0.1 mm spectrometer slit). *Solid line*: vibrational H_2. *Dashed line*: vibrational H_2O. Two theoretical lines are shown separately but not superimposed.
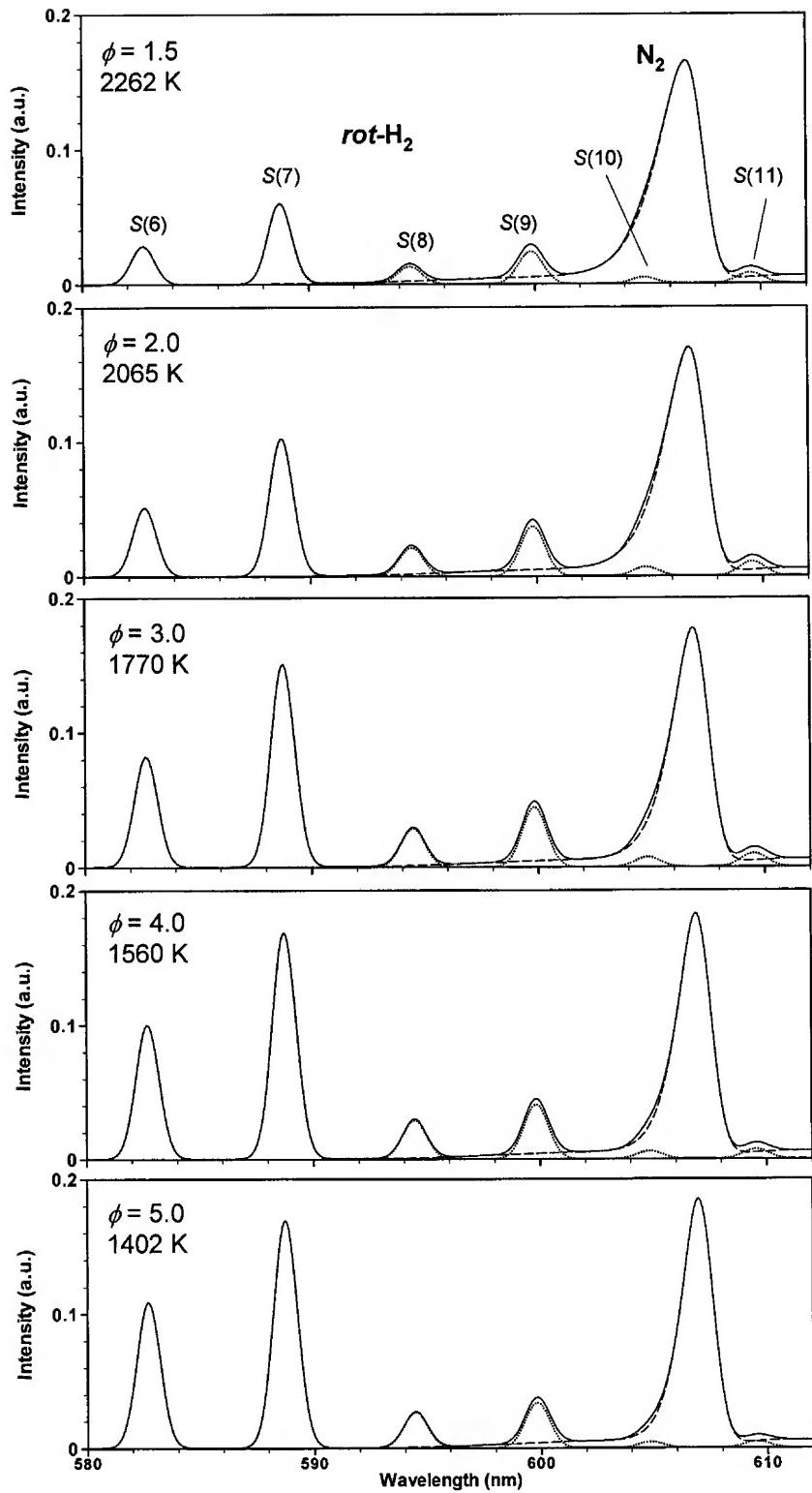
Fig. 8 Calculated vibrational Raman spectra of H_2O and H_2 in 30-atm H_2-air combustion at different equivalence ratios for the five flame cases shown in Table 1 with v_{spec} = 35 cm-1. *Dotted line* is *rot*-H_2, *Dashed line* is N_2, and *Solid line* are superimposed (summation of the two spectra). Intensity is in arbitrary units but in the same scale for all equivalence ratios.
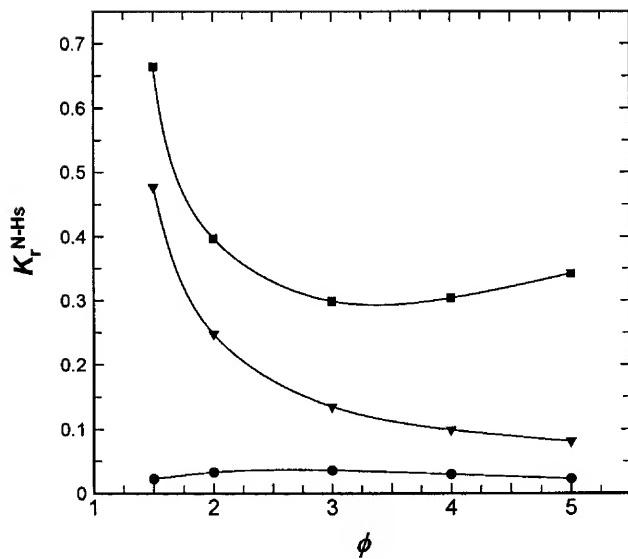
Fig. 9 Cross-talk rate (K_r) between N_2 O-branch and rot-H_2 lines in 30-atm H_2-air combustion at different equivalence ratios, calculated from the spectra shown in Fig. 8 . *Triangles* are K_r^{N-Hs8}; *Squares* are K_r^{N-Hs9}; and *Circles* are K_r^{N-Hs10}. The spectral ranges for the determination of K_r for $S(8)$, $S(9)$, and $S(10)$ are 592.7 ~ 596.3, 598.1 ~ 602.0, 602.3 ~ 609.2 nm, respectively.
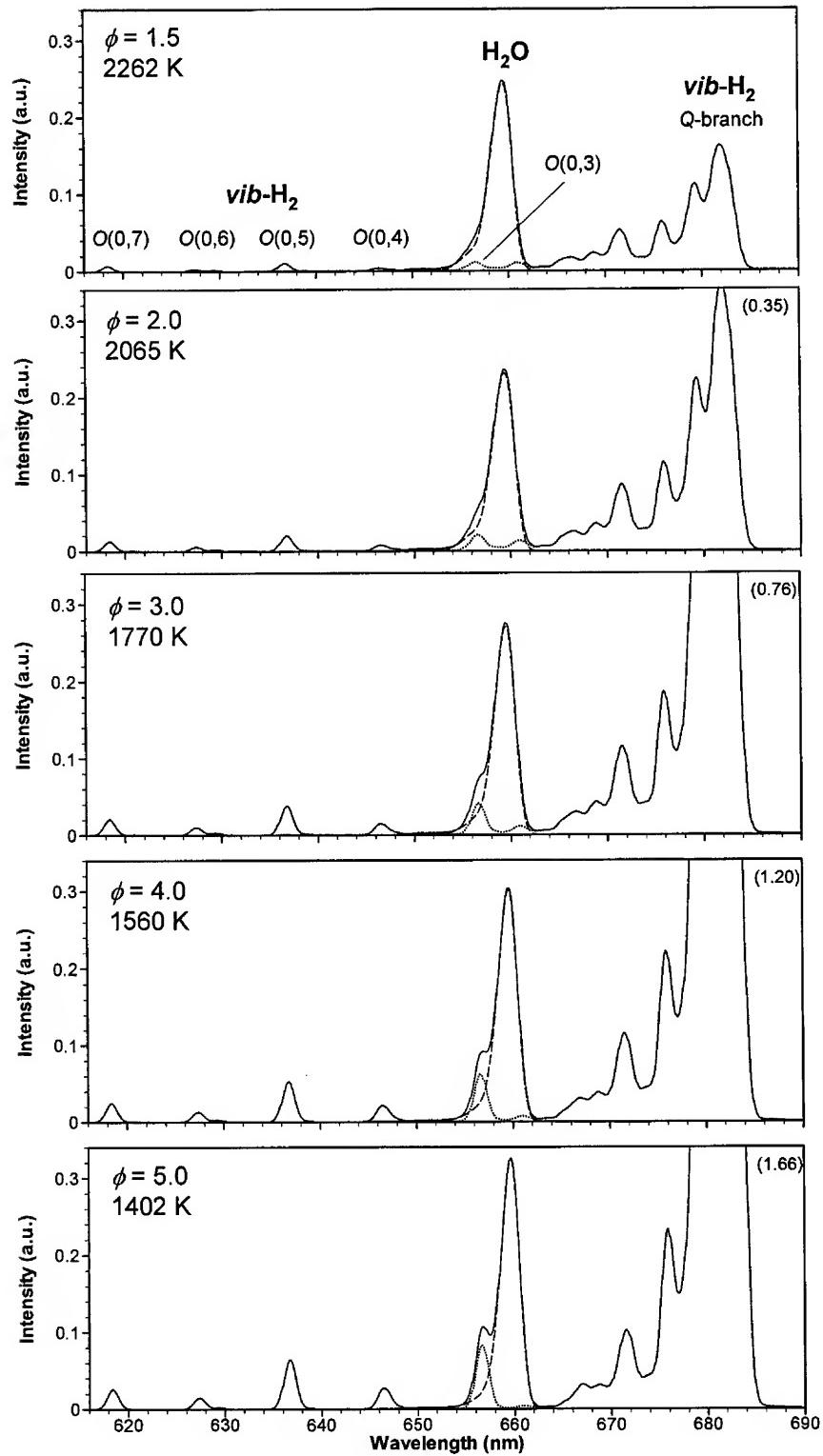
Fig. 10 Calculated Raman spectra of vibrational H_2 and H_2O in 30-atm H_2-air combustion at different equivalence ratios for the five target flames in Table 1 with ν_{spec} = 35 cm^{-1}. *Dotted line* is *vib*-H_2, *Dashed line* is H_2O, and *Solid line* is superimposed line (summation of the two spectra). Intensity is in arbitrary units but in the same scale for all equivalence ratios. Maximum values of *vib*-H_2 for the truncated peaks are included.
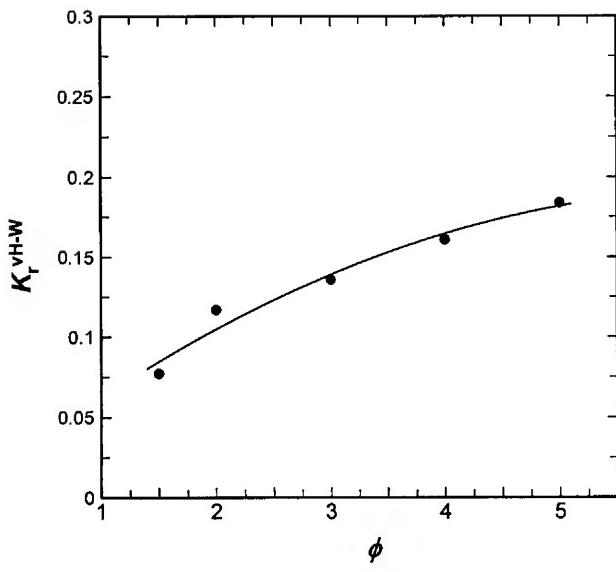
Fig. 11 Cross-talk rate (K_r) between vib-H_2 and H_2O spectrum in 30-atm H_2-air combustion at different equivalence ratios, calculated from spectra shown in Fig. 10. The spectral range for the determination of K_r is from 650.0 to 664.0 nm.
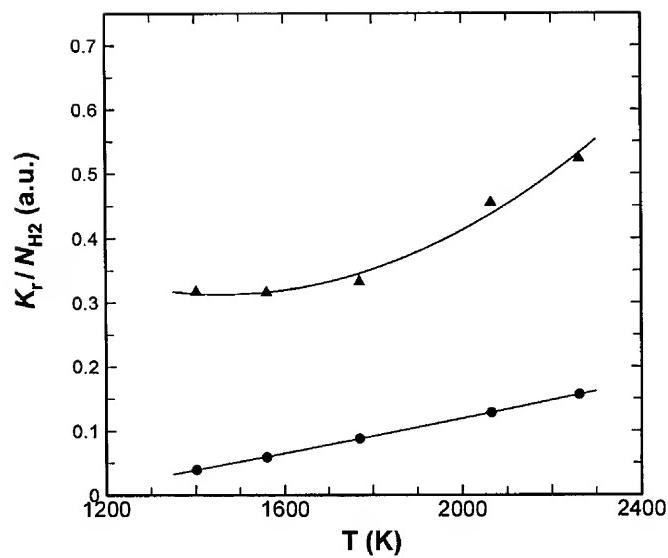
Fig. 12 Temperature dependence of the cross-talk rate (K_r) in 30-atm H_2-air combustion. Here the cross-talk rate is normalized by the adiabatic number density of H_2 for each condition to highlight the true temperature dependence. *Circles* are K_r^{N-Hs10}; *Triangles* are K_r^{vH-W}. Lines are second-order polynomial fit to the points.